ADVANCED MATERIALS INTERFACES
Open Access
www.advmatinterfaces.de

Check for updates

GIWAXS Characterization of Metal–Organic Framework Thin Films and Heterostructures: Quantifying Structure and Orientation

*Jan C. Fischer, Chun Li, Sebastian Hamer, Lars Heinke, Rainer Herges, Bryce S. Richards, and Ian A. Howard**

For optoelectronic applications of metal–organic framework (MOF) thin films, it is important to be able to fabricate films and heterostructures that are highly oriented relative to the substrate's surface normal. However, process optimization to achieve this is difficult without sufficiently detailed structural characterization of the deposited films. It is demonstrated that 2D grazing-incidence wide-angle X-ray scattering (GIWAXS) data from a laboratory system go a long way to providing such characterization and can 1) better test structural models than 1D scans, 2) provide a quantitative estimate—useful for process optimization—of the fraction of the deposited film that has the desired surface-oriented texture (2D powder), and 3) deliver such information as a function of depth into the film—useful for heterostructure characterization. Herein, GIWAXS data collection and analysis are introduced in the context of understanding MOF thin films, then it is shown how the desired oriented fraction (2D powder fraction) of UiO-66 fabricated by vapor-assisted conversion can be increased from 4% to over 95% by minimizing nucleation in solution. Finally, it is demonstrated that heterostructures of UiO-66 and UiO-67 can be grown wherein both layers are highly ordered (UiO-66 83%, UiO-67 >94%) once synthetic protocols are optimized.

1. Introduction

Metal–organic frameworks (MOFs) are of interest for optoelectronic applications because of the variety of unique 3D topologies in which they can hold organic molecules. In a MOF, the intermolecular spacings can be larger than those typically found in a crystal or cocrystal but still small enough that interactions between molecules are observable. In this way, MOFs can be used to control intermolecular interactions in the interesting intermediate coupling regime.[1–4] Combined with the long-range order achievable in MOFs, this could enable applications involving excited-state transport or nonlinear optical properties.[5–9] MOF–MOF heterostructures could offer even better control of excited-state transport and allow new features to be designed into the materials, such as charge carrier separation for applications in photocatalysis or triplet exciton concentration for photon upconversion.[10–12]

When a MOF crystal of sufficient size and quality can be grown, then single crystal X-ray diffraction (XRD) can be used to solve its structure. In the cases when such high-quality crystals are not available, ab initio solution of the structure can also be done based on powder XRD data.[13] However, for thin films of MOFs on a surface,[14] a sample variety that is ideally suited for integration into optoelectronic applications, the small number of unique reflection peaks captured by standard 2θ–θ or grazing incidence XRD out-of-plane and in-plane scans make it challenging to differentiate between different hypotheses for the structure (and completely preclude

J. C. Fischer, B. S. Richards, I. A. Howard
Institute of Microstructure Technology
Karlsruhe Institute of Technology
Hermann-von-Helmholtz-Platz 1, 76344 Eggenstein-Leopoldshafen, Germany
E-mail: ian.howard@kit.edu

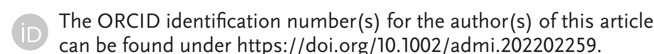
The ORCID identification number(s) for the author(s) of this article can be found under https://doi.org/10.1002/admi.202202259.

© 2023 The Authors. Advanced Materials Interfaces published by Wiley-VCH GmbH. This is an open access article under the terms of the Creative Commons Attribution License, which permits use, distribution and reproduction in any medium, provided the original work is properly cited.

DOI: 10.1002/admi.202202259

C. Li, L. Heinke
Institute of Functional Interfaces
Karlsruhe Institute of Technology
Hermann-von-Helmholtz-Platz 1, 76344 Eggenstein-Leopoldshafen, Germany

S. Hamer, R. Herges
Otto-Diels-Institut für Organische Chemie
Kiel University
Otto-Hahn-Platz 4, D-24118 Kiel, Germany

B. S. Richards, I. A. Howard
Light Technology Institute
Karlsruhe Institute of Technology
Engesserstrasse 13, 76131 Karlsruhe, Germany

any possibility of solving the structure). It is still uncommon to robustly assess the crystal structure and quantify the orientation of MOF films, although both properties are crucial to understand and control for the desired optoelectronic applications of MOF thin films to be realized.

In this contribution we discuss how 2D diffraction patterns assembled from laboratory-scale grazing-incidence wide-angle X-ray scattering (GIWAXS) can be used to determine: 1) the validity of a structural model, 2) the orientation of the thin film growth relative to the substrate surface, and 3) the structure and orientation of the MOF film as a function of depth into the thin film. Although there are several examples of excellent use of GIWAXS in the MOF film community using benchtop,[15–17] or synchrotron beamline systems,[18] the data collection—especially on benchtop/laboratory-scale systems—and subsequent data analysis may be new to many in the field. For this reason, we thoroughly introduce how the data collected at multiple positions of the detector can be stitched together in a way that preserves scattering intensity to allow for subsequent quantitative analysis in reciprocal space (q-space). Also, for the interested reader, we detail GIWAXS data should be transformed to be presented in terms of components of the scattering vector for analysis. Finally, we show how a quantitative estimate of the fraction of the scattering crystallites that are oriented with respect to the surface can be determined. Based on our investigations of UiO-67 and UiO-66 (UiO, Norwegian Universitetet i Oslo) we discuss how insights gained from GIWAXS provide guidance to improve synthetic protocols in terms of better controlling MOF orientation and ultimately achieve >95% of the film in the desired oriented texture for both systems. This then also allows us to make UiO-66-UiO-67 heterostructures by sequential thin film depositions in which a high degree of orientation is maintained throughout the entire heterostructure. With specific reference to engineering MOF thin films and heterostructures for optoelectronic applications, we conclude that GIWAXS is a crucial tool for guiding synthetic protocols toward reliably delivering the structures desired for applications.

2. Results and Discussion

2.1. GIWAXS on MOF Thin Films: Basics

In this section, we introduce the reader to the entire process of collecting, presenting, and analyzing GIWAXS data on MOF films. We describe how data acquired at multiple camera positions are stitched together, and how the composite image from a virtual detector is then projected onto axes describing orthogonal components of the scattering vector for qualitative and quantitative analysis.

First, we introduce the MOF thin film samples. Here, we utilize UiO-66 and UiO-67 thin film samples we fabricated using the vapor-assisted conversion method established by Virmani et al.[17,19] The structure of these UiO MOFs is based on $Zr_6O_4(OH)_4$ clusters that form the secondary building units that are linked together with 12 linear dicarboxylic acid-based linkers, 1,4-benzodicarboxylic acid in the case of UiO-66, and biphenyl-4,4′-dicarboxylic acid in the case of UiO-67. The face-centered cubic structure of these UiO-MOFs is shown in **Figure 1**a. The vapor phase conversion method of synthesis involves mixing a metal precursor, linker, and modulator, in dimethylformamide (DMF) and then pipetting this mixture to form a droplet on a substrate. The substrate sits on stilts in a reaction vessel with solvent and modulator at the bottom. The reaction vessel is then sealed and placed in a 100 °C oven for 3 h, during which time the precursors in the solvent drop on the substrate which should allow the MOF thin film to grow from the surface, whereas the vapor from the solvent and modulator from the bottom of the reaction container help to maintain the volume of the drops (full details of synthesis given in Section S1, Supporting Information). We note that we use 1×1 cm squares cut from (100) Si wafers, but in accordance with previous literature see no difference in synthetic outcome between these and the same substrates covered by 100 nm of evaporated Au.[17,19] The desired outcome is a thin film of crystallites grown from the surface whose $\langle 111 \rangle$ direction is oriented with the surface normal but with random rotation around the $\langle 111 \rangle$ direction in the plane of the film (a so-called 2D powder texture). This is illustrated in Figure 1b. We will consider in the next section why this desired 2D powder texture leads to unique points on the 2D GIWAXS image, whereas a fully isotropic crystallite orientation (without any preferential out-of-plane orientation) leads to rings and how this difference allows the fraction of the sample that is oriented to be determined. However, first, we introduce GIWAXS data collection and processing using the example of a UiO-67 that is the desired 2D powder. We note that as in hybrid perovskites, the X-ray scattering will be dominated by the heavier elements in the material due to their much larger scattering cross-sections,[20] but will see that the diffraction patterns obtained nonetheless contain useful data on both structure and texture.

We use a Bruker D8 Advance diffractometer with a copper X-ray source (at 1600 W power and with a radiation wavelength of 0.154 nm) in GIWAXS configuration equipped an Eiger2 R 500K 2D detector close to the sample position. For a classical 2θ scan (scanning in the out-of-plane direction) under grazing incidence, the detector can be moved on a goniometer to capture images at multiple positions, with the surface normal of the detector always pointing toward the center of the sample. This is illustrated in Figure 1c, where the detector images shown are those for a UiO-67 sample that has a 2D powder texture. To capture the largest range of unique data points in an acquisition in a single detector position, the detector is initially adjusted such that the direct reflection of the X-ray beam hits it in the lower left corner (because of the symmetry of the scattering pattern capturing more than 1 quadrant of the pattern does not reveal new information). To collect further portions of the scattering pattern (extending the out-of-plane scattering angles observed) the detector can be rotated on the goniometer to a higher position. Figure 1c demonstrates the scattering patterns collected for three distinct positions of the detector for this sample (labeled “real detector positions” in the figure).

For reshaping the experimentally acquired data into 2D diffractograms in reciprocal space, we use the open-access software GIXSGUI.[21] Since this program (and most GIWAXS analysis code) considers a 2D image from a single detector, i.e., from a single vertical plane, we first project all acquired images onto a virtual detector directly behind the real goniometer

© 2023 The Authors. Advanced Materials Interfaces published by Wiley-VCH GmbH
21967350, 0, Downloaded from https://onlinelibrary.wiley.com/doi/10.1002/admi.202202259 by Karlsruher Inst F. Technologie, Wiley Online Library on [27/03/2023]. See the Terms and Conditions (https://onlinelibrary.wiley.com/terms-and-conditions) on Wiley Online Library for rules of use; OA articles are governed by the applicable Creative Commons License

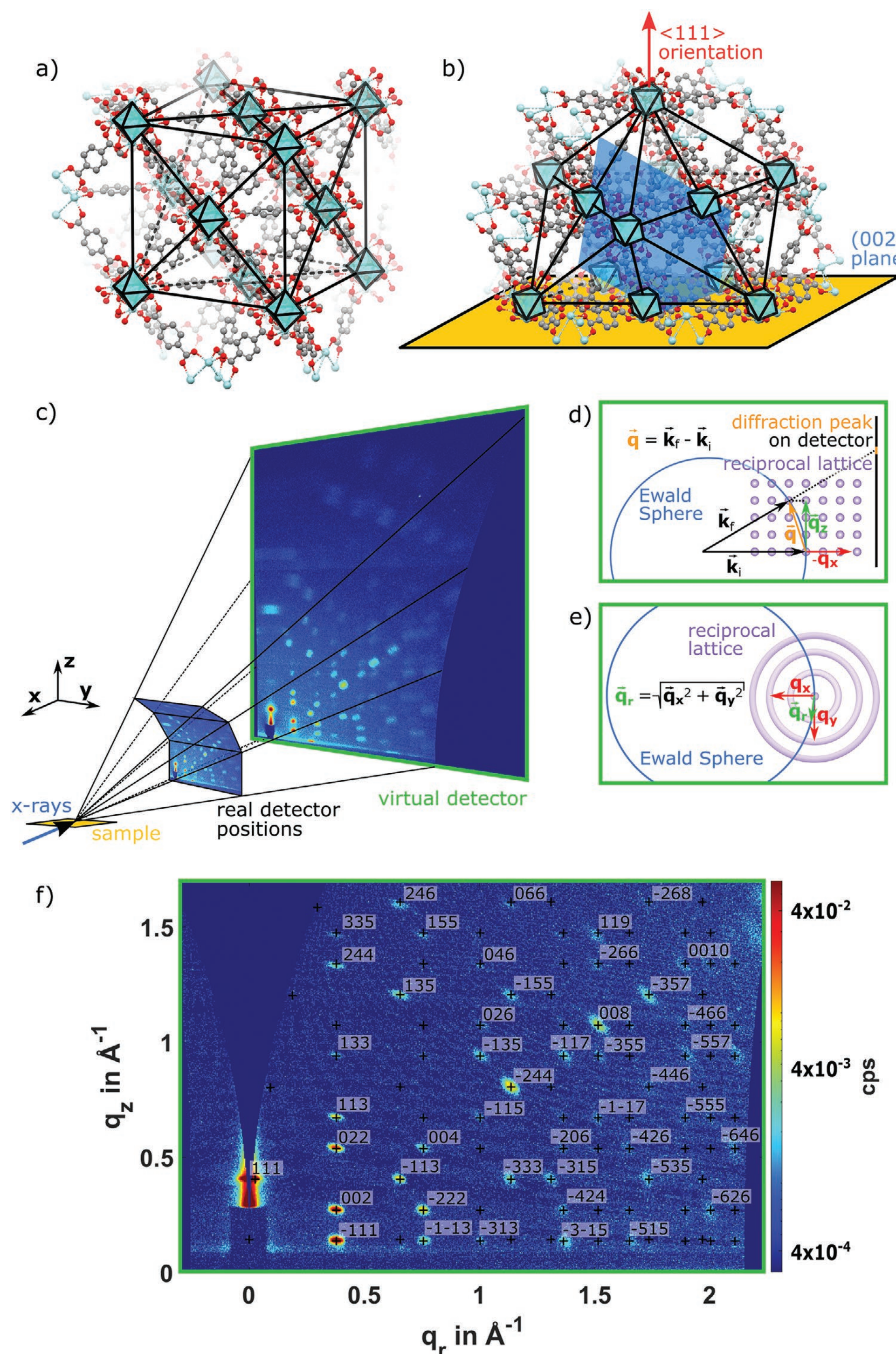

Figure 1. Example of UiO MOF thin film structure and GIWAXS data collection and analysis for a UiO-67 MOF thin film. a) A unit cell of the face-centered cubic UiO structure. b) Example of the desired growth of the UiO structure with its ⟨111⟩ direction parallel to the surface normal. (a,b) Based on the cif-file presented by Valenzano et al.[23] c) GIWAXS measurement showing the scattering images collected at three positions of the real detector, and the projection of these (conserving scattering intensity) onto a planar virtual detector for subsequent analysis. d,e) Illustration of the Ewald sphere defining the scattering vector $\vec{q}$ for elastic X-ray scattering ($|\vec{k}_i| = |\vec{k}_f|$). When $\vec{q}$ bridges two points in reciprocal space, scattering is observed. We wish to express the position of the scattering peaks in terms of $\vec{q_z}$ and $\vec{q_r}$. f) Representation of the image shown on the virtual detector in (c) now in terms of $\vec{q_z}$ and $\vec{q_r}$. The data were acquired with an incidence angle $\alpha_i = 1.00°$. Black crosses indicate calculated peak positions from a literature structure and Laue indices are shown when these correspond to peaks in the observed data.

© 2023 The Authors. Advanced Materials Interfaces published by Wiley-VCH GmbH

21967350, 0, Downloaded from https://onlinelibrary.wiley.com/doi/10.1002/admi.202202259 by Karlsruher Inst F. Technologie, Wiley Online Library on [27/03/2023]. See the Terms and Conditions (https://onlinelibrary.wiley.com/terms-and-conditions) on Wiley Online Library for rules of use; OA articles are governed by the applicable Creative Commons License

circle. This image projected onto the virtual detector can then be treated in GIXSGUI. This is demonstrated in the far right of Figure 1c, where the individual images taken at three different detector positions are projected onto a single, larger vertical surface while conserving the initially measured energy per pixel (see Figure S1 and Section S9, Supporting Information, for the code). Conserving the integral signal intensity is important so that meaningful quantitative analysis (as discussed later) can still be performed. Moreover, at this point, the data are corrected for the polarization of the X-ray source, where in our case the X-ray source is unpolarized.

The next step is to represent the image in terms of components of the scattering vector. This presentation is favored as it is independent of the used X-ray wavelength (source) and extremely useful for qualitative understanding and quantitative analysis of the structure and texture of the thin film. It is important to note that the image measured with the X-ray detector does not directly reflect the reciprocal lattice, it first must be corrected as discussed following.[21] For elastic X-ray scattering, the magnitudes of the incident and final wave vectors ($\vec{k}_\mathrm{i}$ and $\vec{k}_\mathrm{f}$) are the same. The Ewald sphere is a visualizing aid constructed by the wavevectors $\vec{k}_\mathrm{i}$ and $\vec{k}_\mathrm{f}$, with 2D slices of the Ewald sphere shown as blue circles in Figure 1d,e. The vector $\vec{k}_\mathrm{i}$ ends on a reciprocal lattice point, and the scattering vector $\vec{q}$ is the difference between $\vec{k}_\mathrm{f}$ and $\vec{k}_\mathrm{i}$. Scattering occurs when $\vec{q}$ is equal to a reciprocal lattice vector.[22] Equivalently, this means that scattering occurs for the reciprocal lattice points that lie on the Ewald sphere. The locations of the bright scattering points on the detector are given by $\vec{k}_\mathrm{f}$ for the given intersection of a reciprocal lattice point and the Ewald sphere. We wish to represent the scattering pattern in terms of two orthogonal components of $\vec{q}$, namely $\vec{q}_z$ (the z component) and $\vec{q}_r = (\vec{q}_x^2 + \vec{q}_y^2)^{1/2}$, as defined in Figure 1d,e. The curvature of the Ewald sphere has implications that are important for understanding what is measured by GIWAXS, and how the image must be corrected to get the desired representation in reciprocal space.

First, as shown in Figure 1d, the vertical direction of the detector does not purely reflect the q_z axis. The higher up on the detector the scattering is observed, i.e., the larger the scattering angle orthogonal to the substrate, $\beta_\perp$, the larger the component of $\vec{q}_x$ that contributes (beside $\vec{q}_z$) to the total scattering vector, $\vec{q}$, that is observed in the appropriate $\vec{k}_\mathrm{f}$ direction. In other words, the larger the scattering angle, the less the vertical direction on the detector can be approximated as purely $\vec{q}_z$, or pure out-of-plane scattering. Whereas for small-angle scattering the deviation between the vertical direction and $\vec{q}$ can be neglected, in the case of GIWAXS, it needs to be considered. The fundamental inability to measure in the pure $\vec{q}_z$ direction leads to the "missing wedge" in the reciprocal space projection presented in Figure 1f. Thus, even on a qualitative level, transforming data to be viewed in reciprocal space can avoid simple blunders that might be made in considering the direct image captured by the detector. For example, the vertical direction on the detector does not give pure out-of-plane data as a function of angle and it would be a mistake to analyze the raw data in this way.[24,25]

Second, the horizontal axis of the detector does not purely correspond to $\vec{q}_x$ or $\vec{q}_y$, also due to the curvature of the Ewald sphere. However, assuming a 2D powder (a random crystallite orientation with regards to rotation about the z-axis), a meaningful reciprocal space representation can be made by introducing a new auxiliary scattering vector component $\vec{q}_r$. This assumption is generally valid for MOF thin films, except for those prepared by specific routes to introduce long-range order in the substrate plane.[26] The $\vec{q}_r$ vector, shown in Figure 1e, always stays on the surface of the Ewald sphere, and the information about the intersection of the reciprocal lattice with the Ewald sphere is determined by the length of the vector.

We use the GIXSGUI MATLAB toolbox,[21] to reshape the image on the virtual detector that we calculated above (far right in Figure 1c) to the reciprocal space representation presenting scattering intensity in terms of $\vec{q}_z$ and $\vec{q}_r$ (Figure 1f). Figure 1f shows the data of a highly ⟨111⟩-oriented UiO-67 MOF film. A high degree of order and orientation leads to clearly visible, sharp diffraction spots. The substantial number of clearly visible, sharp, and unique diffraction spots is good for testing an existing structural model. The expected positions of the diffraction peaks from a given structure can be determined by the reciprocal lattice generated from a given input structure, plus, the critical angle, α_c, and the absorption coefficient, μ. The α_c and μ were estimated based on density values for UiO-67 powder using the GIXA online tool from TU Wien (elaborated on in Section 2.3; Section S7, Supporting Information).[27,28] The lattice parameters for the face-centered cubic structure were based on those presented for the MOF powder by Chai et al.[10] From this information, the expected peak positions from this structural hypothesis can be calculated by GIXSGUI and compared to experimental data. The black crosses and corresponding Laue index are shown for the calculated diffraction spot locations in Figure 1f. The calculated positions of the diffraction points show excellent agreement with the observed positions of more than ten independent scattering peaks—giving a solid indication that the structural model describes the thin film material well. In terms of a procedure for structural characterization of MOF films, we conclude that comparison of the rich GIWAXS data against structural models derived from single crystal or bulk powder samples is a good approach and sufficient to check whether the structural models as well accurately describe the material structure when grown as a MOF film; and thereby show the same structure is created in the MOF film as in the bulk for this material.

As a brief remark closing this section, the considerable number and distinct pattern of peaks visible in GIWAXS for UiO-type structures make it possible to qualitatively check whether the expected topology is growing or not. For example, we are working on the creation of a UiO-type MOF film with highly dipolar linkers, initially reported by Hamer et al.[29] A vapor-phase assisted synthetic protocol using the dicyanobenzodioxane dipolar rotor linker led to ordered peaks being observed in out-of-plane XRD scans. However, the GIWAXS data of the fabricated structure (in Figure S3, Supporting Information) do not qualitatively agree with that expected from a UiO topology; the wide array of off-axis peaks is missing. Thus, these GIWAXS data can quickly rule out the expected model structure, and clearly indicate when further work must be done to understand the (non-UiO) topology of the surface-grown material.

 © 2023 The Authors. Advanced Materials Interfaces published by Wiley-VCH GmbH

21967350, 0, Downloaded from https://onlinelibrary.wiley.com/doi/10.1002/admi.202202259 by Karlsruher Inst F. Technologie, Wiley Online Library on [27/03/2023]. See the Terms and Conditions (https://onlinelibrary.wiley.com/terms-and-conditions) on Wiley Online Library for rules of use; OA articles are governed by the applicable Creative Commons License

2.2. GIWAXS Analysis to Quantify Oriented Fraction and Optimization of UiO-66 Synthesis

Above, we have considered a UiO-67 sample that is the desired outcome of a MOF film synthesis. That is, the crystallites in the film are oriented with their ⟨111⟩ direction parallel to the surface normal but randomly rotated in the substrate plane (2D powder). Although we could produce highly oriented UiO-67 with reasonable reproducibility, this was initially not the case for the UiO-66 samples where we found that most of the film was not the desired 2D powder but a completely unoriented 3D powder. In this section, we describe the GIWAXS features associated with a 2D and 3D powder, then present how the fraction of the film in the 2D and 3D powder can be quantitatively estimated. Finally, we show how such an understanding of the oriented fraction allowed us to fine-tune the UiO-66 synthesis procedure to give the same 2D powder texture as the UiO-67 data shown above.

A 2D powder texture in which the ⟨111⟩ direction is parallel to the surface normal is schematically illustrated in **Figure 2**a. This cartoon illustration shows nondense truncated cubes for ease of visualization of the scattering, but not to accurately represent a real dense film structure. In this cartoon, the family of {002} planes ((200), (020), and (002)) is parallel to the large area sides of the cubes. Due to the random rotation around the ⟨111⟩ direction of the crystallites, the {002} planes will be randomly rotated with respect to the incoming X-ray beam. This leads to the diffraction signal observed only coming from a subset of the crystallites that happen to have the correct rotation such that elastic scattering of the incoming X-rays is possible from one of the {002} planes. Looking back at Figure 1, this can be understood as only for a given rotation of the reciprocal lattice around $\vec{q}_z$ (i.e., also only for a certain subset of rotations of the real crystal lattice around the z-axis) will the point in reciprocal space that is associated with scattering from one of the planes in the {002} family meet the Ewald sphere and therefore scattering be allowed. Geometrically, we could consider that we are observing the intersection of a toroid on a 2D plane (Figure 2b). The toroid represents the scattering direction of all the 2D powder crystallites, and the elliptical intersection "point" on the plane represents the scattering from the subset of crystallites that happen to have the correct rotation so that we can observe them. To quantify what fraction of the film is made up of crystallites in this desired 2D powder texture, it will be important to multiply the observed scattering signal by a geometric factor that corrects the observed signal for the fraction of the 2D powder that we observe. This correction then makes the signal proportional to the total amount of material in the 2D powder, rather than only the observable fraction of the 2D powder.

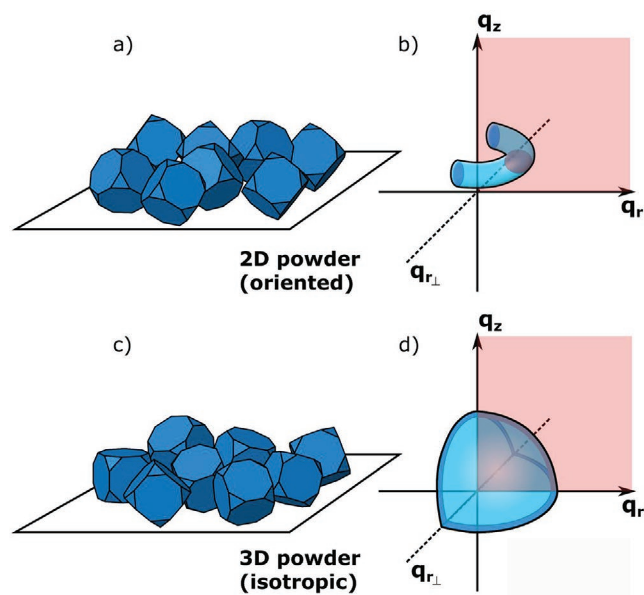

Figure 2. Illustrations to understand scattering from crystallites with a 2D powder texture (their ⟨111⟩ direction oriented parallel to the surface normal but with a random rotation around this axis) versus a 3D powder texture in which the crystallite orientation is isotropic. a) Cartoon illustration of truncated cubes lying on (111) face on the surface but randomly rotated in-plane, a 2D powder texture. The set of planes {002} (used later) can be considered parallel to the large faces of the cubes. b) Torus in reciprocal space corresponding to the total scattering from the set of planes {002} in the 2D powder, and the intersection point with the $q_r - q_z$ plane that corresponds to the observed fraction of the total scattering (i.e., the scattering of the 2D powder whose angle happens to be correct for scattering to be detected in the given experimental geometry). c) 3D powder texture where rotation of the crystal is fully random. d) Sphere in reciprocal space corresponding to total scattering for the set of planes {002} in the isotropic crystallites drawn in (c), and the intersection ring with the $q_r - q_z$ plane that will be observed in the GIWAXS measurements.

Now, as we will see below, we find that if the crystallites do not have a 2D powder texture, they have no preferential orientation and are a randomly oriented 3D powder. This is schematically presented in Figure 2c, where now the truncated cubes do not lie so that their (111) face is aligned with the substrate but are rotated randomly with respect to the substrate normal also. What is observed in GIWAXS if the sample is made of crystallites that have no preferential orientation and are isotopically distributed? Again, looking back to Figure 1, rotation of the reciprocal lattice around the $\vec{q}_x$ axis will cause $\vec{q}$ to remain on the Ewald sphere, with the sum of $\vec{q}_z^2 + \vec{q}_r^2$ remaining constant. This will lead the 3D powder to create a ring of scattering on the $\vec{q}_z$, $\vec{q}_r$ plot. In analogy to the toroid of scattering directions created by all crystal orientations of the 2D powder, the isotropic crystallite orientation distribution will create a sphere, of which we only view the ring created by its intercept with a 2D plane. This is schematically presented in Figure 2d. Again, we observe scattering from a small subset (a smaller subset than in the 2D powder case actually) of the crystallites in the 3D powder that happen to have the correct rotations with respect to the substrate and incoming beam. To quantitatively compare the fraction of material in the 2D and 3D powder we need to correct the observed signals to represent the total scattering due to 2D powder and 3D powder, then find the fraction of the total scattering that each of these populations contributes.

For a qualitative preview of the results, **Figure 3**a,d,g presents the improving GIWAXS data observed as we fine-tune the UiO-66 synthesis intending to avoid nucleation of crystallites in solution (this is discussed in detail following). We can immediately see that as the synthetic procedure is fine-tuned, the resulting film changes drastically in that the scattering rings disappear. Ultimately, the data shown in Figure 3g appear

 © 2023 The Authors. Advanced Materials Interfaces published by Wiley-VCH GmbH

21967350, 0, Downloaded from https://onlinelibrary.wiley.com/doi/10.1002/admi.202202259 by Karlsruher Inst F. Technologie, Wiley Online Library on [27/03/2023]. See the Terms and Conditions (https://onlinelibrary.wiley.com/terms-and-conditions) on Wiley Online Library for rules of use; OA articles are governed by the applicable Creative Commons License

21967350, 0, Downloaded from https://onlinelibrary.wiley.com/doi/10.1002/admi.202202259 by Karlsruher Inst F. Technologie, Wiley Online Library on [27/03/2023]. See the Terms and Conditions (https://onlinelibrary.wiley.com/terms-and-conditions) on Wiley Online Library for rules of use; OA articles are governed by the applicable Creative Commons License

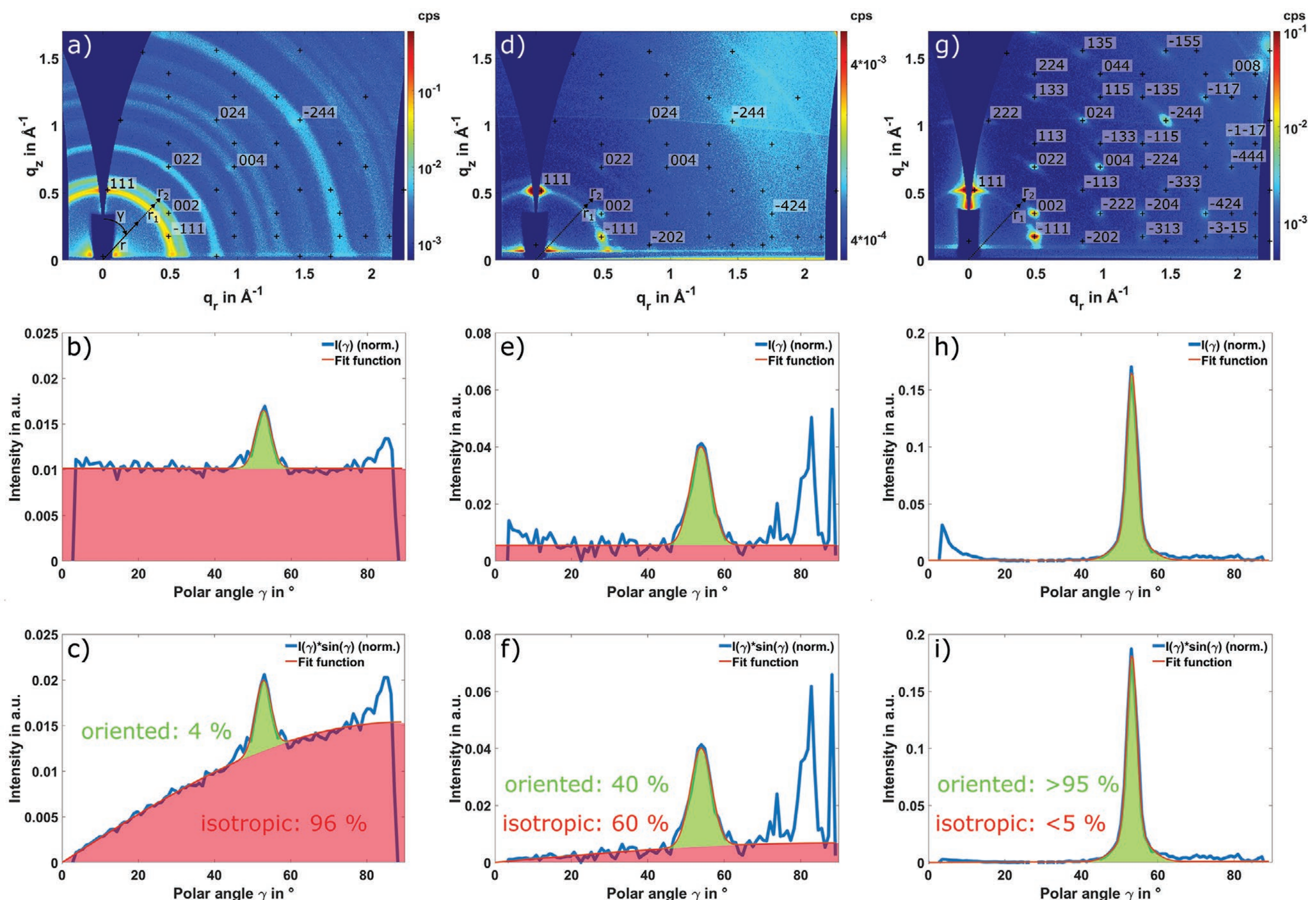

Figure 3. Orientation analysis based on GIWAXS—illustration of fine-tuning UiO-66 synthesis to improve the fraction of the film with desired 2D powder texture. a) GIWAXS of original UiO-66 protocol: predominantly rings superimposed by relatively weak spots ($\alpha_i = 0.20°$). Polar angle, γ, and limits of integration, r_1 and r_2, for generation of the pole figure are shown. b) Pole figure based on (a). The intensity is fit with a constant (coming from the ring caused by the subset of 3D powder crystallites labeled "isotropic"), and Gaussian (coming from the subset of 2D powder population, labeled "oriented"). c) sin(γ) corrected pole corresponding to data in (b) used to estimate that 4% of the film has a 2D powder texture. d) GIWAXS of UiO-66 with protocol adapted to minimize the effect of droplet evaporation during synthesis ($\alpha_i = 0.80°$). e,f) Pole figure and sin (γ) corrected pole figure for (d). g) GIWAXS of UiO-66 with protocol further adapted to minimize time after precursor mixing before insertion in the oven ($\alpha_i = 1.00°$). h,i) Pole figure and sin (γ) corrected pole figure for (g).

of similar quality to that shown in Figure 1f but what are the actual fractions of 2D and 3D powder material in these samples? We will see in the quantitative analysis below that even a small hint of a ring implies a significant fraction of 3D powder in the film.

For quantitative analysis, we will start with the data presented in Figure 3a for the UiO-66 made based on the literature procedure.[17] We will use the scattering from the family of {002} planes as a reporter for the scattering from the 2D and 3D powder populations. As a first step, we prepare a pole figure, as commonly used in descriptions of crystallinity and orientation of a thin film measured by GIWAXS for example for calculating the relative degree of crystallinity between samples, or calculating orientational order parameter (see Section S5, Supporting Information, for more details).[30–33] To generate such a pole figure the scattering intensity is integrated between a minimum and maximum cutoff radius, r_1 and r_2, then presented as a function of the angle to the $\vec{q}_z$ axis, γ. This angle and radii are illustrated in Figure 3a. For the peak and ring that correspond to the scattering from the {002} peak of the UiO-66, we take r_1 to be 0.57 and r_2 to be 0.62 in Figure 3a. To correct for nonsample-related scattering the background (due to air-scattering, etc.) is taken at a slightly larger radius (r_1 = 0.67 and r_2 = 0.73 in Figure 3a) and subtracted from the measured signal. From the pole figure so generated, shown in Figure 3b, we can see that there is scattering from a subset of the fraction of crystallites that have a 3D powder texture. In the pole figure, this is a constant (red area) and is the ring created as described above. Also, we can see that there is scattering from a subset of the crystallites that have a 2D powder texture with their ⟨111⟩ axis aligned to the surface normal. This is the Gaussian peak (green area) and is the point caused by the intersection of the toroid and plane introduced above. The signal near 90° in the pole figure (approaching the horizon) is a Yoneda peak and not considered in the analysis of crystallite orientation. We note that we cannot measure up to $\gamma = 0$ due to the missing wedge. However, as we can choose a peak whose scattering does not lie on the $\vec{q}_z$ axis this is not an impediment, as we can simply

 © 2023 The Authors. Advanced Materials Interfaces published by Wiley-VCH GmbH

and easily extrapolate the constant intensity of the ring to the origin, and the entirety of the intensity in the Gaussian peak is measured.

Now, to make the comparison between the total scattering due to the material in the 2D and 3D powder texture populations, we need to introduce a correction to the pole figure to account for the fraction of scattering signal observed for the 2D and 3D powders at each γ. As in the calculations for the relative degree of crystallinity (see Section S5, Supporting Information), this can be accomplished by multiplying the measured intensity, $I(\gamma)$, by $\sin(\gamma)$. $\sin(\gamma)$ gives the radius to generate the surface of a revolution, created by rotating the point defined by $I(\gamma)$ around the $\vec{q}_z$ axis. This corrects the observed scattering signal to the total scattering signal that would be observed if all crystallites of the 2D and 3D powder textures were visible for a given γ. This correction is valid given the crystallites have an isotropic orientation with respect to the surface normal, which both the 2D and 3D powder textures do. In other words, the toroid and sphere shown in Figure 2 both have radial symmetry and are recreated when $I(\gamma)$ is multiplied by the $\sin(\gamma)$ correction. Exactly this procedure (fitting of pole figure, then correction of pole figure by $\sin(\gamma)$) has been previously used to establish the volume fraction of conjugated polymer crystallites in a thin film in edge-on, face-on, and isotropically oriented textures, so this analysis has precedent.[32,34,35]

The $\sin(\gamma)$ corrected pole figure that now represents the total scattering from the 2D and 3D powder population is shown in Figure 3c, with the areas corresponding to the oriented and isotropic contributions noted. These are generated by multiplying the fits in the previous pole figure with $\sin(\gamma)$ as well. In the $\sin(\gamma)$ corrected pole figure, the intensity represents the scattering intensity from all crystallites, not only those in the correct orientation to create visible scattering. Thus, we can simply integrate the areas corresponding to the oriented and isotropic contributions in the $\sin(\gamma)$ corrected pole figure to get a ratio of the oriented to isotropic scattering contribution. For the data presented in Figure 3c, the ratio of the area due to oriented crystallite scattering to the total area indicates that 4% of the crystallites is oriented. In contrast to 1D out-of-plane scans, this ability of GIWAXS to easily distinguish oriented and isotropic crystallite contributions to scattering is a key advantage of this technique in terms of analysis of MOF films.

To summarize, the fraction of crystallites in the desired 2D powder texture can be quantitatively determined by considering a pole figure examining diffraction from a given set of planes. Here, it is advantageous for the diffraction peak from these planes in a 2D powder texture to be well resolved in the GIWAXS data (not near the missing wedge or horizon). Hence our selection of the {002} reflections is as a good reporter peak. We find that for our MOF thin films the contribution to the pole figure of oriented and isotropic crystallite fractions can be easily established by fitting with a Gaussian and constant line, respectively. Depending on the peak shape of the oriented feature, we either fit it with a single Gaussian or with the sum of two Gaussians with differing widths and amplitudes but a constant center. The preceding fits can then be corrected to account for all material in the textures by multiplying with $\sin(\gamma)$, and the result is integrated to determine the fraction of oriented crystallites in the sample. As a warning, if there is more than one diffraction spot located on the isotropic ring, all of them need to be considered for orientation evaluation with consideration of the reciprocal lattice symmetry. It is simplest to choose a radius with a single peak if possible (as we have done). As a final caveat, an aspect to keep in mind is the depth of the film probed by the incidence angle chosen. The data in this section were taken at incidence angles such that the entirety of the film was probed, so the estimates of the 2D powder fraction reflect the whole film thickness. This will be discussed in more detail in the following section.

As a side note to the interested reader, if a peak along $\vec{q}_z$ is desired for the pole figure analysis, obtaining a complete pole figure up to $\gamma = 0$ for a specific $\vec{q}_z$ could be possible based on some reconfiguration of the experimental conditions, namely, taking GIWAXS data under local specular reflection conditions.[25,31,36] In this experimental workaround, to get data all the way to the $\vec{q}_z$ axis (equivalently all the way to $\gamma = 0$ on the pole figure) at a given radius only, one could measure the sample again at a greater incidence angle chosen to rotate the Ewald sphere sufficiently that the reciprocal lattice point corresponding to the desired peak intercepts the Ewald sphere on the true $\vec{q}_z$ axis. Technically, this means setting the incidence angle of the X-ray source equal to the scattering angle (extrapolated from the above measurement) for the desired peak at $\vec{q}_r = 0$. This trick could allow a complete pole figure to be generated at a given $\vec{q}_z$.[25,36]

Clearly, the result that only 4% of the film is in the targetted desired 2D powder texture for this UiO-66 synthesis is not desirable. For comparison, no constant offset from 3D crystallites is observed for the UiO-67 film shown in Figure 1f (see polar plots in Figure S4). To estimate a lower bound for the fraction of the film with 2D powder texture, we take the standard deviation of the "baseline" points to estimate the maximum fraction of 3D powder that we would be unable to see. From this, we can conclude that >96% of the good quality UiO-67 film shown in Figure 1f is in the desired 2D powder texture.

To fine-tune the synthesis of UiO-66 we hypothesized that nucleation and growth of crystallites in solution that then fall onto the substrate (landing with a random orientation) could be a cause of the 3D powder texture. We recall that in the vapor phase synthesis method used a droplet containing precursors and modulator is placed on a substrate inside a sealed vessel that also contains solvent and modulator in its base. This is then heated to start the reaction. Depending on the volume of the droplet placed on the substrate, the substrate area, and the gas volume in the reaction vessel, the rate of evaporation of the droplet will vary. As the droplet evaporates, the concentrations of the precursors within the droplets increase, and the probability of homogeneous nucleation and formation of MOF crystallites within the solution phase increases. These could then drop to the surface and be incorporated into the oriented film growing from the surface, explaining an isotropic component. This hypothesis is supported by our observations from depth profiling revealing that the surface of the films is often less oriented than the bulk (which is discussed in the next section).

To test the hypothesis that nucleation in solution may be decreasing the fraction of oriented crystallites, we aimed to decrease the rate with which the concentration of the precursors in the droplet increase after it is placed in the oven. This should

© 2023 The Authors. Advanced Materials Interfaces published by Wiley-VCH GmbH

21967350, 0, Downloaded from https://onlinelibrary.wiley.com/doi/10.1002/admi.202202259 by Karlsruher Inst F. Technologie, Wiley Online Library on [27/03/2023]. See the Terms and Conditions (https://onlinelibrary.wiley.com/terms-and-conditions) on Wiley Online Library for rules of use; OA articles are governed by the applicable Creative Commons License

decrease the probability to nucleate in solution and favor more ordered growth from the surface. To do this we used a reaction vessel with a broader base (250 mL GLS80 bottle instead of 100 mL GL45) to increase the surface area of the solvent and more quickly increase the vapor pressure of the solvent upon introduction to the oven (and therefore decrease the rate of evaporation of the droplet). Second, we increased the volume of the droplet on the substrate for the synthesis from 40 to 80 µL. The total larger volume of the droplet on the surface will mean that a given rate of evaporation will have a lower effect on the relative decrease in the droplet volume, meaning that the concentration will stay uniform longer. These changes in the synthesis improved the degree of orientation of the MOF film as presented in Figure 3d, and the corresponding pole figure and sin (χ) corrected pole figure in Figure 3e,f. The overall fraction of the film with a 2D powder texture is improved to 40%.

Finally, we consider the "hidden variable" of the length of time between mixing the precursors to initiating synthesis in the oven. Previously this was on the time scale of several hours. Although no significant powder formation in solution was visible during this time, potentially, clusters of precursors could be gradually formed that ease nucleation and growth in solution. To minimize this, we followed the procedure as above to minimize nucleation in solution but in addition, we mixed the precursors directly before depositing the droplets onto the substrates then immediately sealed the vessels and loaded the substrates into the oven. This meant that less than 5 min elapsed between mixing the precursors and the start of the MOF thin film synthesis. The results of the UiO-66 thin film made in this way are shown in Figure 3g with the corresponding pole figure and sin(χ) corrected pole figure in Figure 3h,i. Now only peaks corresponding to the indicated Laue indices are observed, like the UiO-67 sample shown in Figure 1f. As no clear indication of a constant offset in the pole figure can be seen, we again estimate the largest offset that we could not observe from the standard deviation of the baseline. Due to the slightly worse signal-to-noise in this measurement, this allows us to conclude that >95% of the scattering comes from the 2D powder texture so that the sample indeed has the desired high degree of surface orientation.

To summarize this section, we show that the vapor phase conversion method can easily lead to a mixture of crystallites with the desired 2D powder texture and unwanted 3D powder texture. The dynamics of the synthetic protocol are nontrivial, but our simple tuning experiments above indicate that minimization of nucleation of crystallites in solution that then grow and fall onto the substrate is likely important for achieving a high fraction of crystallites that are in the desired (oriented) 2D powder texture. We believe that GIWAXS will be an essential tool for studying MOF thin film texture and enabling increasingly robust synthetic protocols to be developed.

2.3. GIWAXS on MOF Films: Variation of Angle of Incidence and Depth Profiling

As alluded to in the previous section, one further interesting aspect of the GIWAXS technique is the ability to change the depth of the film that the X-rays penetrate by varying the angle of incidence, α_i. An introduction to how the penetration depth changes on a smooth thin film is given in Section S7 of the Supporting Information. For angles below the critical angle (roughly less than 0.1° for MOF thin films), the X-ray beam is totally externally reflected and only the first few nanometers of the film should be measured through the evanescent field. For angles above the critical angle, the X-rays penetrate through the film, and the entirety of the film quickly becomes measured. The strong caveat to this is that the roughness of the film can compromise such a simple analysis, as it locally can significantly alter the angle of incidence and thereby change the volumes of the film considered (especially at very small angles where some protruding features could lead to X-rays penetrating these protruding volumes).[20] Surface roughness in perovskite films has been observed to make the total scattering intensity less dependent on the incidence angle than expected.[20]

Figure 4a,c compares GIWAXS measurements on a UiO-67 sample with an α_i = 0.05° (corresponding to a penetration depth of only 6 nm in a smooth film) and one with an α_i = 1°, corresponding to a penetration depth of 26.8 µm (by far exceeding the actual thin film thickness and therefore meaning the whole film will be probed). This UiO-67 is made with nominally the same procedure as that shown in Figure 1f but shows a somewhat worse 2D powder fraction (this was prepared before the time between precursor mixing and deposition was carefully controlled—it is an honest indication that synthetic protocols whose outcome are more robust against minor variations in parameters are desirable).

Of interest here, the GIWAXS data are significantly different for the two angles of incidence. The smaller angle of incidence probes a volume of material comprised of a much smaller fraction of the desired surface-oriented 2D powder than the bulk of the film (probed by the 1° angle of incidence). The sin (χ) corrected pole figures for these two GIWAXS measurements are shown in Figure 4b,d. From these, the fraction of oriented crystallites considering only the surface is found to be 10%, whereas the fraction of oriented crystallites when considering the whole film is 57%. The same tendency is also observed in UiO-66 films, with subcritical angles of incidence measuring volumes of the film that have reduced fractions of the desired 2D powder texture (Figure S6, Supporting Information).

This observation is interesting, and we posit two possible causes. The first is that nucleation in solution could get more problematic as the drop evaporates, and lead to more crystallites formed in solution and dropping onto the surface as the synthesis nears its end. In this case, the 3D textured material could be enriched at the top layers of the film. This hypothesis is shown in Figure 4e. However, as similar observations of less 2D powder texture fraction at subcritical incidence angles are made also for films that are created with procedures that minimize the change in drop volume during deposition, it could also be that the few crystallites that are created in solution and drop onto the film tend to be large enough that they protrude out of the film surface. This could lead this volume of material to be penetrated by the X-ray beam even when most of the smoother film is probed only by the evanescent wave. This hypothesis is shown in Figure 4f.

© 2023 The Authors. Advanced Materials Interfaces published by Wiley-VCH GmbH

21967350, 0, Downloaded from https://onlinelibrary.wiley.com/doi/10.1002/admi.202202259 by Karlsruher Inst F. Technologie, Wiley Online Library on [27/03/2023]. See the Terms and Conditions (https://onlinelibrary.wiley.com/terms-and-conditions) on Wiley Online Library for rules of use; OA articles are governed by the applicable Creative Commons License

21967350, 0, Downloaded from https://onlinelibrary.wiley.com/doi/10.1002/admi.202202259 by Karlsruher Inst F. Technologie, Wiley Online Library on [27/03/2023]. See the Terms and Conditions (https://onlinelibrary.wiley.com/terms-and-conditions) on Wiley Online Library for rules of use; OA articles are governed by the applicable Creative Commons License

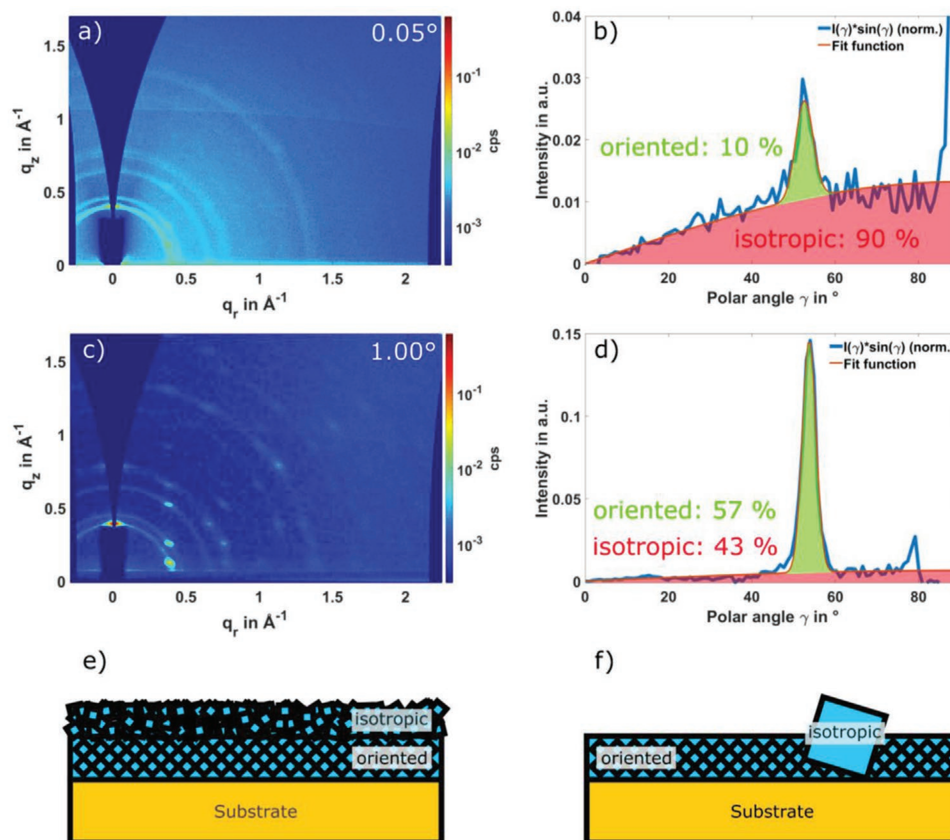

Figure 4. GIWAXS depth profiling of UiO-67. a) GIWAXS at $\alpha_i = 0.05°$ (surface measurement). b) sin (γ) corrected {002} pole figure of the surface data in (a). c) GIWAXS at $\alpha_i = 1°$ (bulk measurement). d) sin (γ) corrected {002} pole figure of the bulk data in (c). e,f) Schematic illustrations of how sample roughness could affect GIWAXS signal as a function of α_i. e) A nominally smooth film where the whole film would be probed with the evanescent wave even at small α_i and therefore the α_i scan will be more directly related to a depth profile. f) A large isotropic crystal protruding from the surface which will have a different α_i than the flat film, and thereby be penetrated by X-rays even when the flat film is only probed by the evanescent wave.

Both hypotheses will be considered when we scan the angle of incidence on MOF thin film heterostructures presented below, where we will also show the value of scanning angle of incidence for analyzing MOF thin films. Finally, we also note that the area of the sample probed increases with decreasing angle of incidence, so some spatial inhomogeneity in film quality could also play a role in changing the GIWAXS pattern as a function of angle.

2.4. GIWAXS on UiO-66/UiO-67 Heterostructures

For optoelectronic applications, forming a heterostructure by growing one MOF film from the surface of another is of interest. In this section, we present a GIWAXS analysis of two exemplary heterostructures we find of interest in terms of demonstrating the utility of GIWAXS for gaining understanding.

In the first example, before we controlled the time of precursor mixing prior to initiation of synthesis, we investigated growing UiO-66 from a "templating" UiO-67 layer to see whether this could improve the orientation of UiO-66. To grow the heterostructure, we fabricated a UiO-67 thin film with the standard procedure, then deposited the UiO-66 precursor solution onto the UiO-67 coated substrate and followed the same procedure as for the film shown in Figure 3d. The result of this synthesis is shown in **Figure 5**a,b. A sequence of GIWAXS measurements was performed from low to high angles of incidence to gain insight into the composition of the MOF film stack (full scan in Figure S7, Supporting Information). It is clear to see these first probe only the UiO-66 overlayer, then as α_i increases the UiO-67 underlayer is probed as well. At the lowest angle of incidence only rings corresponding to UiO-66 crystallites with a 3D powder texture are visible (Figure S7, Supporting Information). By an α_i of 0.07°, 3D powder texture of UiO-66 still dominates the scattering, but a weak signal from UiO-67 in a 2D powder texture can start to be observed. At an α_i of 0.16° (Figure 5b), the whole film is probed and distinct peaks corresponding to oriented (2D powder) UiO-67 are clearly visible in addition to the rings from the UiO-66. The UiO-67 scattering peaks coincide with the simulated diffraction pattern denoted by pink crosses (as calculated based on a ⟨111⟩ surface-oriented UiO-67 structure as in Figure 1f). The ring radii for the UiO-66 scattering are also labeled by yellow arrows corresponding to the crystal planes that are responsible for this scattering in a 3D powder texture.

For a more quantitative analysis, the sin (γ) corrected pole figures for analyzing the {002} diffraction in the α_i of 0.16° dataset (whole film) are shown in Figure 5c,d. Although the

 © 2023 The Authors. Advanced Materials Interfaces published by Wiley-VCH GmbH

21967350, 0, Downloaded from https://onlinelibrary.wiley.com/doi/10.1002/admi.202202259 by Karlsruher Inst F. Technologie, Wiley Online Library on [27/03/2023]. See the Terms and Conditions (https://onlinelibrary.wiley.com/terms-and-conditions) on Wiley Online Library for rules of use; OA articles are governed by the applicable Creative Commons License

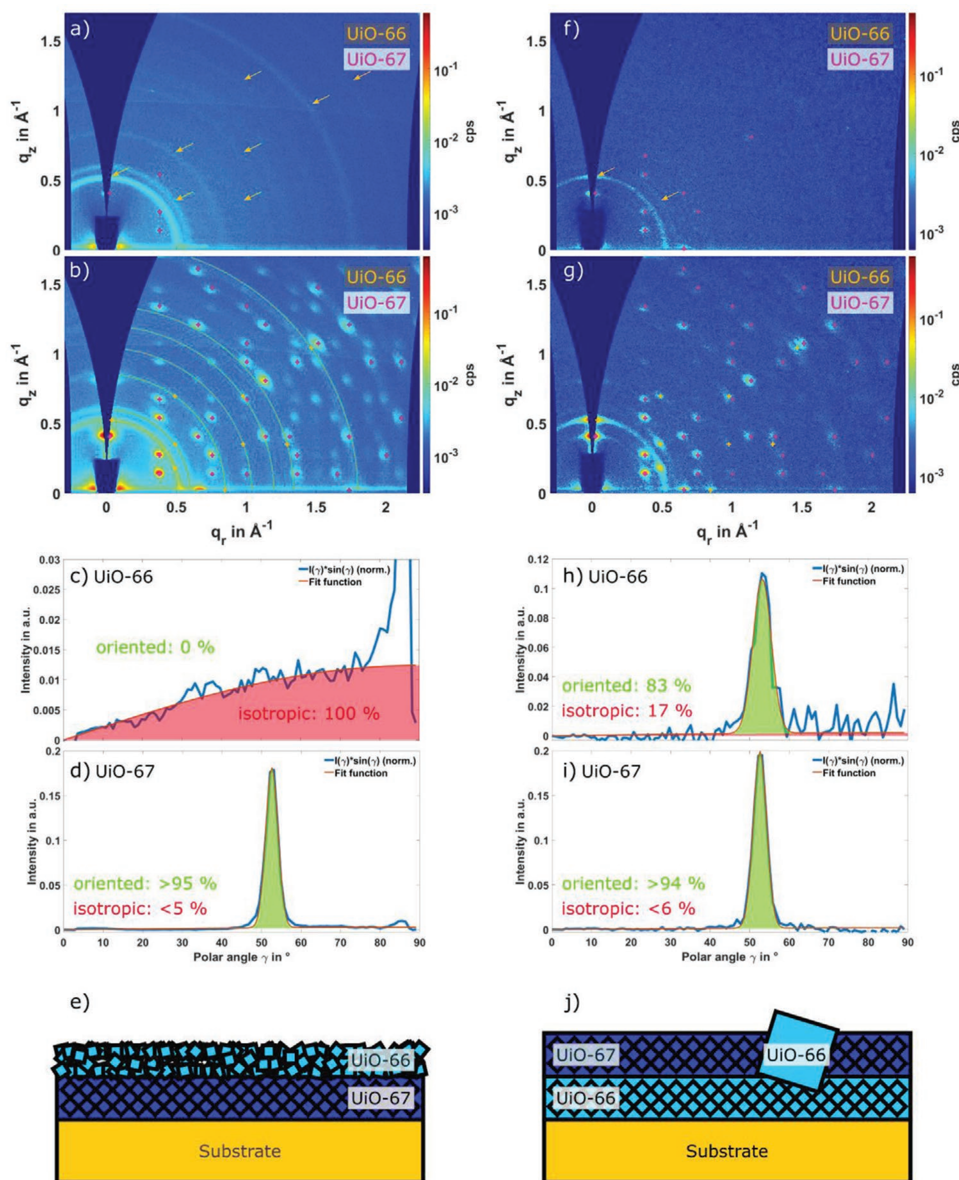

Figure 5. UiO heterostructures. a) UiO-66 on UiO-67 GIWAXS at $\alpha_i = 0.07°$ and b) $\alpha_i = 0.16°$. Both MOF layers are clearly visible. The high number of diffraction spots indicates a well-preserved highly oriented UiO-67 bottom layer. c,d) sin (γ) corrected {002} polar plots of (c) UiO-66 and (d) UiO-67 taken from (b). e) A heterostructure schematic that is consistent with the GIWAXS data in (a)–(d). f) UiO-67 on UiO-66 GIWAXS at $\alpha_i = 0.08°$ and g) $\alpha_i = 0.16°$. h,i) sin (γ) corrected {002} polar plots of (h) UiO-66 and (i) UiO-67 taken from (g). j) A heterostructure schematic that is consistent with the GIWAXS data in (f)–(i).

UiO-67 remains highly oriented (>95% in the desired 2D powder) the orientation of the overgrown UiO-66 layer was negligible. A schematic of the heterostructure texture based on these findings is shown in Figure 5e. A scanning electron microscope (SEM) cross-section (Figure S8a, Supporting Information) corroborates the GIWAXS findings. In the SEM image, the 100 nm Au layer on top of the Si substrate is visible, followed by the 150 nm dense UiO-67 layer and then a 100 nm UiO-66 layer that is less dense and oriented. So, in this case, despite an excellently oriented substrate, even the improved UiO-66 deposition did not generate the desired oriented heterostructure. But the ability of GIWAXS to provide information on the thin films on both sides of the heterostructure is clearly demonstrated.

For the second example of GIWAXS on a heterostructure, we take the best recipe for UiO-66 (shown in Figure 3g) as the first layer then grow a UiO-67 layer on top of it. In this case, the subcritical incidence angle α_i of 0.08° (Figure 5f) shows distinct peaks corresponding to the UiO-67 structure in the desired 2D powder texture (indicated in pink) but also surprisingly a clear signal that corresponds to UiO-66 with a 3D powder texture (indicated in yellow). For the further images under the critical angle, this trend continues (see Figure S9, Supporting Information). The well oriented top layer of UiO-67 becomes more and

© 2023 The Authors. Advanced Materials Interfaces published by Wiley-VCH GmbH

ADVANCED MATERIALS INTERFACES
Open Access
www.advmatinterfaces.de

21967350, 0, Downloaded from https://onlinelibrary.wiley.com/doi/10.1002/admi.202202259 by Karlsruher Inst F. Technologie, Wiley Online Library on [27/03/2023]. See the Terms and Conditions (https://onlinelibrary.wiley.com/terms-and-conditions) on Wiley Online Library for rules of use; OA articles are governed by the applicable Creative Commons License

more clearly visible, but puzzlingly a poorly ordered portion of the "bottom" UiO-66 layer is also visible. When α_i reaches 0.16° and the whole depth of the heterostructure is probed, clearly ordered UiO-66 peaks become strongly visible in addition to those from the UiO-67. The simulated positions for the UiO-66 peaks are shown in yellow and those for the UiO-67 in pink in Figure 5g. sin (γ) corrected pole figures for the {002} family of planes for the UiO-66 and 67 are shown in Figure 5h,i and we estimate that the ordered fraction (2D powder texture) in the film is satisfyingly high for both the UiO-66 (83%) and the UiO-67 (>94%).

Now the question arises, why is a poorly ordered fraction of the UiO-66 visible "on-top" of the UiO-67 for low (subcritical) α_i? We hypothesize a structure such as that schematically presented in Figure 5j. A few UiO-66 crystallites are still nucleated in solution, and grow to a considerable size (≈100 nm) before falling onto the 2D powder UiO-66 layer. Even after the subsequent UiO-67 deposition, these occasional solution-nucleated crystals of UiO-66 could stick out from the rest of the film, and therefore have a significantly different α_i than the rest of the film, allowing them to provide a larger signal due to X-ray penetration into their bulk while the denser flatter parts of the film are only probed by the evanescent wave. The SEM of this heterostructure is shown in Figure S8b of the Supporting Information. A dense UiO-66 underlayer is observable, upon which an ordered UiO-67 can be seen with lateral grain size on the order of 100 nm. However, protruding from the top UiO-67 layer is occasionally large octahedral crystals (>100 nm length). In conjunction with the corresponding GIWAXS data, we conclude that these are the UiO-66 crystals that cause the isotropic rings already appearing at low incidence angle. This is a nice example of how GIWAXS and SEM can complement each other. The presence of some larger solution-nucleated crystals in this case for our most optimized UiO-66 synthesis does indicate the reality that further work on increasing the reproducibility in the quite dynamic vapor-assisted conversion is an important goal for the community.

3. Conclusions

We have presented how GIWAXS on MOF thin films can be collected on a laboratory scale diffractometer system and explained how the collected data can be processed to a form useful for qualitative and quantitative understanding of MOF thin films. We hope that this will be useful for a broader uptake of GIWAXS in the MOF thin film community, which we believe will be essential for the development of synthetic protocols that yield MOF thin films of the desired oriented textures in a fashion that is more tolerant to minor process fluctuations.

In terms of specific results on the benchmark UiO systems deposited via a vapor phase conversion approach, we find that the desired surface-oriented 2D powder texture can often be accompanied by a 3D powder texture that we hypothesize could be due to nucleation in solution. We find that the deposition of highly oriented UiO-67 is more robust than that of UiO-66, although high-quality films of UiO-66 could be obtained after the synthetic protocol was fine-tuned with the aim of minimizing nucleation in solution. We have obtained samples of UiO-67 and UiO-66 wherein no constant offset from 3D textured material could be observed in the pole figure. The fraction in the surface-oriented 2D texture is close to 100% for such samples, and we estimate the lower bound for the oriented fraction by taking the standard deviation in the baseline of the pole figure to estimate the highest fraction of 3D texture that could be present, but we would not be able to resolve. This leads us to conclude that the fraction of the desired 2D texture must be >96% and >95% for the UiO-67 and UiO-66, respectively (due to slightly different signal-to-noise levels in the measurements). However, we note that further adjustments to the vapor phase conversion protocol should still be explored to improve the robustness to uncontrolled fluctuations in synthetic conditions.

We then show that variation of the angle of incidence is useful for characterizing both MOF thin films and their heterostructures. In some cases, depth profiling can be achieved with this method, for example, a UiO-66 layer with an undesired 3D powder texture can be seen at angles below the critical angle, well before the well-ordered UiO-67 underlayer can be seen. However, in rough samples or in cases of islanded growth, where the angle of incidence can vary due to protrusion of crystallites from the surface, care must be taken in interpreting the change in the GIWAXS pattern as a function of incidence angle. For example, in this case, penetrative X-ray scattering from the protrusions might be superimposed on evanescent probing of the surface layer. We propose that this may occur on the best quality heterostructure that we grow of a UiO-66 base layer (83% in oriented texture) with a UiO-67 layer grown on top (>94% in oriented texture). In any case, we show that GIWAXS characterization is an essential asset for understanding MOF thin film heterostructures.

In summary, we show that GIWAXS on MOF thin films is 1) highly beneficial for testing structural models (as many more unique diffraction peaks are visible than the limited number in out-of-plane or in-plane scans), 2) can give a qualitative and quantitative indication of the ratio of the desired oriented 2D texture to the undesired 3D texture (based on the intensity of the spot versus ring for diffraction from a set of planes), and 3) can also provide information on the sample topology due to scanning the angle of incidence (which is of especial use in pursuing high-quality heterostructures). These aspects of structural understanding are of high importance for the development of optoelectronic quality MOF thin films, and we anticipate a continued uptake of GIWAXS for MOF film examination will be of significant assistance in driving the further development of such materials.

Supporting Information

Supporting Information is available from the Wiley Online Library or from the author.

Acknowledgements

The authors gratefully acknowledge the DFG for funding through the priority program SPP 1928 COORNETS, as well as the Helmholtz Association for funding through i) HEMF, ii) the MTET program (Materials and Technologies for the Energy Transition)—Topic

© 2023 The Authors. Advanced Materials Interfaces published by Wiley-VCH GmbH

1—Photovoltaics (38.01.05), and iii) the recruitment initiative of B.S.R. Furthermore, the authors want to thank the Karlsruhe School of Optics and Photonics (KSOP) and the Ministry of Science, Research and the Arts of Baden-Württemberg (Excellence Initiative II) for supporting this work. The authors thank Gowtham Arivanandhan and Yunzhe Jiang for their help in performing SEM measurements.

Open access funding enabled and organized by Projekt DEAL.

Conflict of Interest

The authors declare no conflict of interest.

Data Availability Statement

The data that support the findings of this study are openly available in UiO GIWAXS at https://git.scc.kit.edu/xi6101/uiogiwaxs, reference number 35930.

Keywords

crystallite orientation, depth-profiling, GIWAXS, heterostructures, oriented metal–organic framework thin films

Received: October 21, 2022
Revised: January 24, 2023
Published online:

[1] V. Stavila, A. A. Talin, M. D. Allendorf, *Chem. Soc. Rev.* **2014**, *43*, 5994.
[2] R. Haldar, L. Heinke, C. Wöll, *Adv. Mater.* **2020**, *32*, 1905227.
[3] R. Haldar, M. Kozlowska, M. Ganschow, S. Ghosh, M. Jakoby, H. Chen, F. Ghalami, W. Xie, S. Heidrich, Y. Tsutsui, J. Freudenberg, S. Seki, I. A. Howard, B. S. Richards, U. H. F. Bunz, M. Elstner, W. Wenzel, C. Wöll, *Chem. Sci.* **2021**, *12*, 4477.
[4] A. T. Castner, H. Su, E. Svensson Grape, A. K. Inge, B. A. Johnson, M. S. G. Ahlquist, S. Ott, *J. Am. Chem. Soc.* **2022**, *144*, 5910.
[5] A. A. Talin, A. Centrone, A. C. Ford, M. E. Foster, V. Stavila, P. Haney, R. A. Kinney, V. Szalai, F. el Gabaly, H. P. Yoon, F. Léonard, M. D. Allendorf, *Science* **2014**, *343*, 66.
[6] Q. Zhang, C. Zhang, L. Cao, Z. Wang, B. An, Z. Lin, R. Huang, Z. Zhang, C. Wang, W. Lin, *J. Am. Chem. Soc.* **2016**, *138*, 5308.
[7] Y. Sun, H. Li, X. Gao, Z. Yu, Z. Huang, C. Zhang, *Adv. Opt. Mater.* **2021**, *9*, 2100622.
[8] X. Jiang, L. Zhang, S. Liu, Y. Zhang, Z. He, W. Li, F. Zhang, Y. Shi, L. Wei, Y. Li, Q. Wen, J. Li, J. Feng, S. Ruan, Y. J. Zeng, X. Zhu, Y. Lu, H. Zhang, *Adv. Opt. Mater.* **2018**, *6*, 1800561.
[9] M. Adams, M. Kozlowska, N. Baroni, M. Oldenburg, R. Ma, D. Busko, A. Turshatov, G. Emandi, M. O. Senge, R. Haldar, C. Wöll, G. U. Nienhaus, B. S. Richards, I. A. Howard, *ACS Appl. Mater. Interfaces* **2019**, *11*, 15688.
[10] L. Chai, J. Pan, Y. Hu, J. Qian, M. Hong, *Small* **2021**, *17*, 2100607.
[11] Y. Yu, S. Li, L. Huang, J. Yu, H. Zhang, S. Song, T. Zeng, *Catal. Commun.* **2021**, *150*, 106270.
[12] M. Oldenburg, A. Turshatov, D. Busko, S. Wollgarten, M. Adams, N. Baroni, A. Welle, E. Redel, C. Wöll, B. S. Richards, I. A. Howard, *Adv. Mater.* **2016**, *28*, 8477.
[13] J. Martí-Rujas, *Dalton Trans.* **2020**, *49*, 13897.
[14] L. Heinke, H. Gliemann, P. Tremouilhac, C. Wöll, in *The Chemistry of Metal–Organic Frameworks: Synthesis, Characterization, and Applications*, (Ed: S. Kaskel), 1st Edn., Wiley-VCH Verlag GmbH & Co, KGaA, Weinheim **2016**.
[15] P. I. Scheurle, A. Mähringer, A. Biewald, A. Hartschuh, T. Bein, D. D. Medina, *Chem. Mater.* **2021**, *33*, 5896.
[16] B. Rühle, E. Virmani, H. Engelke, F. M. Hinterholzinger, T. von Zons, B. Brosent, T. Bein, A. Godt, S. Wuttke, *Chemistry* **2019**, *25*, 6349.
[17] E. Virmani, J. M. Rotter, A. Mähringer, T. von Zons, A. Godt, T. Bein, S. Wuttke, D. D. Medina, *J. Am. Chem. Soc.* **2018**, *140*, 4812.
[18] S. Hou, W. Li, S. Watzele, R. M. Kluge, S. Xue, S. Yin, X. Jiang, M. Döblinger, A. Welle, B. Garlyyev, M. Koch, P. Müller-Buschbaum, C. Wöll, A. S. Bandarenka, R. A. Fischer, *Adv. Mater.* **2021**, *33*, 2103218.
[19] J. H. Cavka, S. Jakobsen, U. Olsbye, N. Guillou, C. Lamberti, S. Bordiga, K. P Lillerud, *J. Am. Chem. Soc.* **2008**, *130*, 13850.
[20] W. L. Tan, C. R. McNeill, *Appl. Phys. Rev.* **2022**, *9*, 021310.
[21] Z. Jiang, *J. Appl. Crystallogr.* **2015**, *48*, 917.
[22] J. Als-Nielsen, D. McMorrow, *Elements of Modern X-Ray Physics*, John Wiley and Sons, Oxford **2011**.
[23] L. Valenzano, B. Civalleri, S. Chavan, S. Bordiga, M. H. Nilsen, S. Jakobsen, K. P. Lillerud, C. Lamberti, *Chem. Mater.* **2011**, *23*, 1700.
[24] P. Müller-Buschbaum, *Adv. Mater.* **2014**, *26*, 7692.
[25] J. L. Baker, L. H. Jimison, S. Mannsfeld, S. Volkman, S. Yin, V. Subramanian, A. Salleo, A. P. Alivisatos, M. F. Toney, *Langmuir* **2010**, *26*, 9146.
[26] P. Falcaro, K. Okada, T. Hara, K. Ikigaki, Y. Tokudome, A. W. Thornton, A. J. Hill, T. Williams, C. Doonan, M. Takahashi, *Nat. Mater.* **2017**, *16*, 342.
[27] D. Ingerle, Glancing Incidence X-ray Analysis (GIXA) X-ray Tools, https://gixa.ati.tuwien.ac.at/tools/penetrationdepth.xhtml (accessed: September 2022).
[28] J. A. Villajos, *C* **2022**, *8*, 5.
[29] S. Hamer, F. Röhricht, M. Jakoby, I. A. Howard, X. Zhang, C. Näther, R. Herges, *Beilstein J. Org. Chem.* **2019**, *15*, 1331.
[30] A. Mahmood, J. L. Wang, *Sol. RRL* **2020**, *4*, 2000337.
[31] J. Rivnay, S. C. B. Mannsfeld, C. E. Miller, A. Salleo, M. F. Toney, *Chem. Rev.* **2012**, *112*, 5488.
[32] M. R. Hammond, R. J. Kline, A. A. Herzing, L. J. Richter, D. S. Germack, H. W. Ro, C. L. Soles, D. A. Fischer, T. Xu, L. Yu, M. F. Toney, D. M. Delongchamp, *ACS Nano* **2011**, *5*, 8248.
[33] R.-J. Roe, *Methods of X-Ray and Neutron Scattering in Polymer Science*, Oxford University Press, New York **2000**.
[34] J. E. Allen, K. G. Yager, H. Hlaing, C. Y. Nam, B. M. Ocko, C. T. Black, *Appl. Phys. Lett.* **2011**, *99*, 163301.
[35] D. E. Johnston, K. G. Yager, H. Hlaing, X. Lu, B. M. Ocko, C. T. Black, *ACS Nano* **2014**, *8*, 243.
[36] L. H. Jimison, A. Salleo, M. L. Chabinyc, D. P. Bernstein, M. F. Toney, *Phys. Rev. B: Condens. Matter Mater. Phys.* **2008**, *78*, 125319.

© 2023 The Authors. Advanced Materials Interfaces published by Wiley-VCH GmbH

21967350, 0, Downloaded from https://onlinelibrary.wiley.com/doi/10.1002/admi.202202259 by Karlsruher Inst F. Technologie, Wiley Online Library on [27/03/2023]. See the Terms and Conditions (https://onlinelibrary.wiley.com/terms-and-conditions) on Wiley Online Library for rules of use; OA articles are governed by the applicable Creative Commons License